


Two-Shot Calibration Method for Phase-Only Spatial Light Modulators with Generalized Spatial Differentiator

Junyi Huang, Tengfeng Zhu, and Zhichao Ruan*

¹*Interdisciplinary Center of Quantum Information, State Key Laboratory of Modern Optical Instrumentation, and Zhejiang Province Key Laboratory of Quantum Technology and Device of Physics Department, Zhejiang University, Hangzhou 310027, China*

 (Received 30 June 2020; revised 28 August 2020; accepted 22 October 2020; published 17 November 2020)

For phase-only spatial light modulators (SLMs), it is necessary to calibrate phase-response curves in various applications with light wavefront shaping. Here we develop a method to calibrate the global phase-response curve, based on the generalized optical spatial differentiation. We show that by only setting two specific profiles in SLM and analyzing the light reflected by a planar interface under cross-polarization conditions, the phase delay can be evaluated from two shots of intensity images. In comparison with conventional interferometric or diffractive approaches, we experimentally demonstrate that the present method enables *in situ* calibration and takes advantages of simple process and high stability. Besides, the method can also be used to calibrate the phase-response curve of each single pixel.

DOI: [10.1103/PhysRevApplied.14.054040](https://doi.org/10.1103/PhysRevApplied.14.054040)

I. INTRODUCTION

Spatial light modulators (SLMs) are fundamental devices in optical applications for wavefront manipulations. In recent years, phase-only spatial light modulators, especially based on liquid crystal, have been widely used in various fields, e.g., optical computing tasks [1–6], quantum optics [7], optical micromanipulation and tweezers [8,9], and microscopy [10]. Potentially, spatial light modulators are also suggested in the applications of optical coherence tomography [11], time evolution of topological quantum states [12,13], and ultrafast polariton and plasmon polariton procedures [14,15]. In these applications, it is necessary for the first step to calibrate phase-response curves of SLMs, which ensures precise control of desired phase delay.

The principle of SLM calibration is to convert modulated phase delays into detectable intensity variations. Currently, a number of methods have been developed based on interferometric or diffractive approaches. The calibration performance strongly relies on two factors: mechanical stability and complexity of data processing. With well-established interferometers generating interference fringes, the phase delay by SLM can be easily retrieved by analyzing the variation of the fringe patterns [16–19], but the interferometers are sensitive to mechanical or environmental disturbances and thus require multiple measurements to reduce deviations. In order to ensure high stability, the methods based on common-path

interferometry [20,21] and diffraction [22–24] have been proposed. They are simple and stable but with the price of time to change the input grayscale values and take a number of shots. In addition, other calibration methods are developed based on interferometric [25] and diffractive patterns [26]. These techniques are stable and need only one or a few shots, but with the strong demand of image processing for data fitting to extract phase delays. In general, it is still desirable to develop SLM calibration techniques, which have high mechanical stability but with less need for data processing.

In this paper, we propose a two-shot method to calibrate the global phase-response curve of SLM, based on the generalized spatial differentiation. Recently, optical analog computation of spatial differentiation has attracted particular attention because of its advantages of high throughput and real-time computing in a single shot. Various optical analog computing devices have been designed for spatial differentiation of scalar fields simply with linear polarization, e.g., using metamaterials and metasurfaces [27–36], dielectric interfaces [4,5,37], periodic slabs [38–43], and plasmonic structures [3,44–46]. In particular, with the spin Hall effect of light, we have experimentally demonstrated the generalized spatial differentiation: during reflection at a single planar interface, the spatial differentiation perpendicular to the incident plane can be realized by analyzing the polarization state orthogonal to that of the incident light [4]. Moreover, since the spin Hall effect is an intrinsic effect of light, such spatial differentiation generally occurs at any planar interface, regardless of material compositions, incident angles, or light wavelengths.

*zhichao@zju.edu.cn

In comparison with the current interferometric or diffractive methods, the proposed method is to load only two different patterns in SLM and directly measure each intensity image after optically performing spatial differentiation, without complex image processing. Therefore, the calibration process is much more efficient and stable. We validate the method by comparing the calibrated phase-response curve with the method by using the well-known two-beam interference technique [16] and experimentally demonstrate the improvement of diffraction efficiency in application of holography. In addition, with multiple shots the proposed method can be straightforwardly extended to a calibration method for each single pixel. Since the proposed calibration setup is only with common imaging systems and polarization analysis, it can be easily adapted to deployed setups. In particular, our method works *in situ* in the cases that the deployed setups have imaging systems to project the phase-delay image loaded by SLMs, e.g., in the applications of all-optical neural network [1] and encoding complex fields with a phase-only SLM [6].

II. METHODOLOGY

Our calibration method is based on the generalized spatial differentiation shown in Fig. 1. Suppose that an incident electric field $E_{\text{in}}(x, y)$ obliquely illuminates on a planar interface with an incident angle θ_0 . We note that since the spin Hall effect of light is independent of material compositions [4], the reflective interface can be general, e.g., a planar mirror or a glass slab. Here the polarizer $P1$ is used to prepare the incident field with p (s) polarization, while the polarizer $P2$ is used to analyze the s (p) polarization, which is orthogonal to the initial one. After such cross-polarization analysis, the output field is proportional to the spatial differentiation of the input field [4]:

$$E_{\text{out}}(x, y) = C[E_{\text{in}}(x, y + \delta) - E_{\text{in}}(x, y - \delta)], \quad (1)$$

where $C = i(r_p + r_s)/4$, and r_p and r_s are Fresnel's reflection coefficients of the p - and s -polarized plane waves with the incident angle θ_0 , respectively. Equation (1) can be understood by taking into account that the initial linearly polarized field can be decomposed into the right- and left-handed circular polarization states (the blue and the yellow beams in Fig. 1, respectively). Due to the spin Hall effect of light [4,47], after reflection at the planar interface, two such circularly polarized beams experience the opposite shifts of $\pm\delta$ in the transverse y direction, respectively, shown as $E_{\text{in}}(x, y \pm \delta)$, where $\delta = 2 \cot \theta_0 / k_0$, and k_0 is the wave number in the incident medium. With the orthogonal polarizer $P2$, the output field is contributed by the destructive interference between two circularly polarized beams, which corresponds to the minus sign in the middle of Eq. (1). Since the spin Hall effect is an intrinsic effect of light, the spatial differentiation is general and

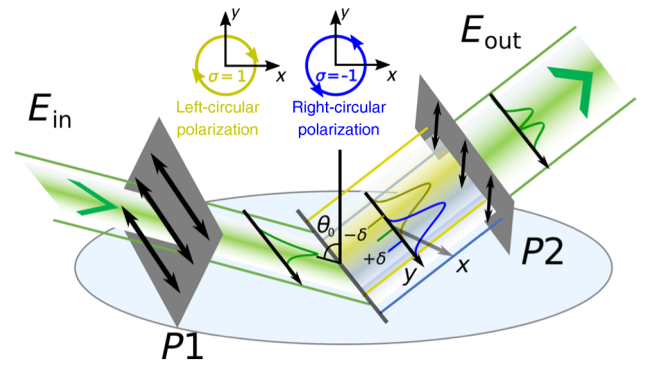


FIG. 1. Schematic of the generalized spatial differentiation with two polarizers and one planar interface. A paraxial beam obliquely illuminates on a planar interface with an incident angle θ_0 . Two polarizers $P1$ and $P2$ are used to enable polarization analysis under cross-polarization conditions indicated with double-head arrows, e.g., s - and p -polarization states here, respectively. The initial field prepared by $P1$ can be decomposed into right- and left-handed circular polarization states, which experience the opposite transverse shifts of $\pm\delta$ during the reflection, respectively. $P2$ is used to enable destructive interference between the two states. Here x and y are the beam-profile coordinates for the incident and reflected light, which are parallel and perpendicular to the incident plane, respectively. The incident and reflected beams have the vector electric fields E_{in} and E_{out} dominating in the transversal direction. We note that since the spin Hall effect of light is independent of material compositions, the reflective interface can be general, e.g., a planar mirror or a glass slab.

independent of material compositions, incident angles, or light wavelengths [4,47].

To calibrate a phase-only SLM, here we consider an optical system schematically shown in Fig. 2(a). The goal is to quantitatively determine the relation between the phase delays induced by the SLM and the corresponding input grayscale values. We assume that SLM manufacturers have corrected the wavefront and enabled the phase-delay response independent of pixels. Here a reflective SLM is illuminated by a collimated monochromatic laser beam with linear polarization. We suppose that the collimated laser beam has an amplitude A , and the SLM delays the phase of a single incident field segment by φ , as $A \rightarrow Ae^{i\varphi}$. With a conjugate imaging system consisting of lenses $L1$ and $L2$, the phase-modulated field $E_{\text{in}}(x, y) = A(x, y)e^{i\varphi(x, y)}$ is projected to the spatial differentiator, consisting of a planar interface and polarizers $P1$ and $P2$. Here the coordinates x and y in the SLM are defined in accordance with the spatial differentiation system as shown in Fig. 1. The incident angle is chosen such that the shift δ is much smaller than the SLM pixel size. According to Eq. (1), the reflected field after the spatial differentiation is

$$E_{\text{out}}(x, y) = CA(x, y) [e^{i\varphi(x, y + \delta)} - e^{i\varphi(x, y - \delta)}]. \quad (2)$$

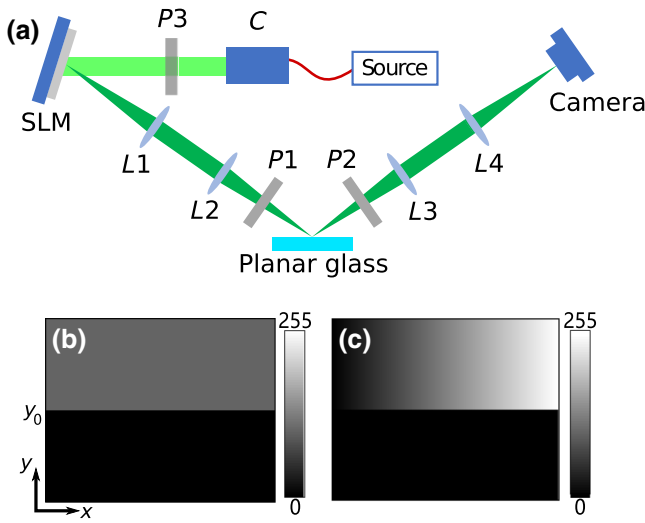


FIG. 2. Schematic of the phase calibration of phase-only SLMs. (a) The setup: C , collimator; P , polarizer; L , lens. The light source is connected to the collimator through a fiber. The generalized spatial differentiator consists of $P1$, $P2$, and planar glass. (b),(c) Input grayscale images in the first and second shot, respectively. The lower part $y < y_0$ has the fixed value of zero for both images. The upper part $y \geq y_0$ for (b) has a uniform nonzero value, while the values for (c) increase linearly from 0 to 255 with the unitary step along the x direction.

With a conjugate imaging system ($L3$ and $L4$), the output intensity distribution is measured by a camera.

Next we show a two-shot method to evaluate the phase delay with the optical spatial differentiator. In the first step, we set a grayscale image as Fig. 2(b) in SLM, which consists of two parts: the lower part $y < y_0$ has the value fixed to zero, while the upper part $y \geq y_0$ is uniform with a nonzero value. In this case, according to Eq. (2), the measured output intensity distribution $I_1(x)$ at $y = y_0$ is

$$I_1(x) = B |C|^2 A^2(x), \quad (3)$$

where B is a constant related to the phase contrast between the lower and upper parts and can be determined by the maximal normalized intensity of Eq. (5).

In the second step, we set a grayscale image as Fig. 2(c), which consists of two parts: although the lower part $y < y_0$ has the same value of zero as shown in Fig. 2(b), the upper part for $y \geq y_0$ has the grayscale values gradually increasing from zero to the maximum with the unitary step, which means that the modulated phases $\varphi(x)$ at the upper part can cover the range from 0 to 2π . Thus, according to Eq. (2), the measured output intensity distribution at $y = y_0$ is

$$I_2(x) = 2|C|^2 A^2(x) \{1 - \cos[\varphi(x)]\}. \quad (4)$$

To determine the phase delay, we normalize the two measured intensities as

$$\tilde{I}(x) = \frac{I_2(x)}{I_1(x)} = \frac{2 - 2\cos[\varphi(x)]}{B}. \quad (5)$$

Since the phases $\varphi(x)$ cover the range from 0 to 2π , the intensity distribution reaches the maximum value \tilde{I}_{\max} of $\tilde{I}(x)$ where $\varphi(x) = \pi$. By determining \tilde{I}_{\max} and the corresponding position x_{\max} , we obtain the coefficient $B = 4/\tilde{I}_{\max}$ and evaluate the other phases by Eq. (5). For example, when $x < x_{\max}$, we have

$$\varphi(x) = \arccos \left[1 - \frac{2\tilde{I}(x)}{\tilde{I}_{\max}} \right]. \quad (6)$$

We can also unwrap the phases for the other ranges by taking into account the phase continuity increasing with the grayscale value.

Since the grayscale value is associated with the position x , we finally calibrate the SLM by determining the one-to-one correspondence between the phase delays and the input grayscale values. Furthermore, for the linear dependence, the phase-response curve can be massaged by looking up and rescaling the voltage setting table. Moreover, the experimental setup and the method can also be used to calibrate the SLM for other wavelengths, because the spatial differentiation generally occurs without the wavelength limitation.

III. RESULT

To demonstrate the calibration process, we calibrate a SLM (Holoeye PLUTO-NIR-011) at the wavelength $\lambda = 532$ nm. As shown in Fig. 2(a), a Gaussian laser beam is collimated through a rotating ground glass diffuser in order to eliminate speckles and enhance the image quality. The incident beam covers the whole SLM and the incident angle is less than 5° to assure the phase-only modulation. A conjugate imaging system consisting of lenses $L1$ ($f = 500$ mm) and $L2$ ($f = 60$ mm) projects the modulated field to a BK7 glass surface with the incident angle $\theta_0 = 45^\circ$, resulting in a transverse shift $\delta = 169$ nm. The polarizers $P1$ and $P2$ are used to prepare and analyze the s - and p -polarization states, respectively. The other conjugate imaging system consisting of $L3$ ($f = 100$ mm) and $L4$ ($f = 400$ mm) projects the reflected field to a beam profiler (Ophir SP620).

We perform the two-shot method by measuring the intensity distributions $I_1(x)$ and $I_2(x)$. First, we set the input grayscale value pattern in SLM [Fig. 2(b)]. We note that out of the pattern, the grayscale value is continually uniform along y direction such that no differentiation signal is generated according to Eq. (1). For a large calibration area, there are 768 pixels along the x direction. Moreover,

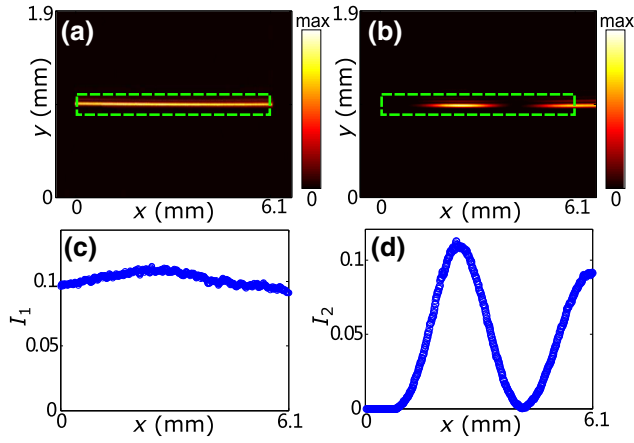


FIG. 3. (a),(b) The measured intensity distributions in the two shots where the pattern in $0 < x < 6.1$ corresponds to the input image of SLM as Figs. 2(b) and 2(c), respectively. (c),(d) $I_1(x)$ and $I_2(x)$ calculated by summing the intensities along the y direction within the region outlined by the green dashed line from (a) to (b).

in order to improve the signal-to-noise ratio, the grayscale value at the upper part is set to enable relatively strong intensity of $I_1(x)$, which does not require the quantitative value of the phase delay in prior. Figure 3(a) shows the measured output intensity distribution. In agreement with Eq. (1), the output fields only have strong intensities at the boundary between the upper and the lower parts, which correspond to spatial differentiation along the y direction. We note that since the grayscale value is continually uniform along the y direction outside the pattern in Fig. 2(b), there are no output intensities generated except at $y = y_0$. Therefore, we can locate the pixels of two endpoints of the bright line in CCD and map them to the two endpoints at $y = y_0$ of the pattern in SLM. In this way, for each x value, Fig. 3(c) shows the intensity distribution $I_1(x)$, by summing the intensities along the y direction, within the region outlined by the green dashed line in Fig. 3(a).

Next, we set the input grayscale image of the SLM as Fig. 2(c). Here each three adjacent pixels are treated as a subgroup and set with the same grayscale value, in accordance with the first pattern setting. We keep the grayscale values out of the pattern continuous with the inside to make the phase continuous in x direction, which can reduce the influence of diffraction on the output intensity distribution at the two endpoints, i.e., $x = 0$ and $x = 6.1$ mm at the boundary. The output intensity distribution is shown in Fig. 3(b). Correspondingly, $I_2(x)$ shown in Fig. 3(d) is also acquired by summing the intensities along the y direction within the region.

Now we determine the phase-response curve from the normalized intensity. According to Eq. (5), the result \tilde{I} is calculated by normalizing the measured $I_1(x)$ and $I_2(x)$, which is shown as the blue circle line in Fig. 4(a). On

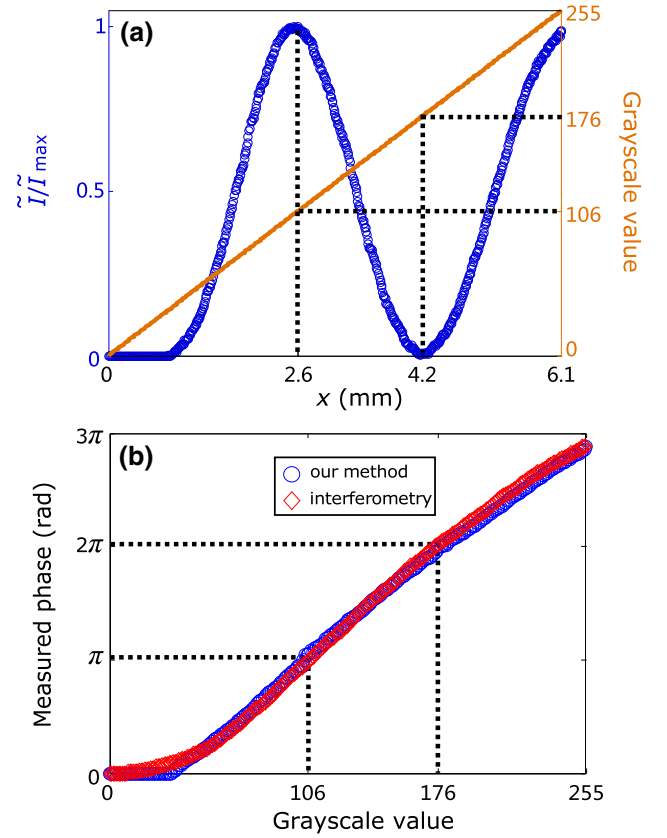


FIG. 4. (a) $\tilde{I}(x)/\tilde{I}_{\max}$ (blue circle line) and the input grayscale values (orange line) as a function of the position x . (b) The phase-response curve measured with our method (blue circle line) and two-beam interference method (red rhombus line).

the other hand, the input grayscale values are determined and associated with the positions x , as the orange line in Fig. 4(a). Therefore, for each x position, we can calculate the phase delay by Eq. (6) and the corresponding grayscale value. For example, for $x = 2.6$ mm, the phase delay is $\varphi = \pi$ where $\tilde{I}(x) = \tilde{I}_{\max}$, and the corresponding grayscale value is 106. Also at the position where $\tilde{I}(x)$ reaches the minimal value at $x = 4.2$ mm, we can determine a phase delay $\varphi = 2\pi$ corresponding to the grayscale value of 176. By processing all the other positions, we finally determine the one-to-one correspondence between the phases φ and the input grayscale values, which is shown as the blue circle line in Fig. 4(b).

To verify the calibration method, we also measure the phase-response curve by using the two-beam interference

TABLE I. Number of shots and time consumption for two methods.

Method	Number of shots	Time consumption
Spatial differentiation	2	0.3 s
Two-beam interference	256	14 s

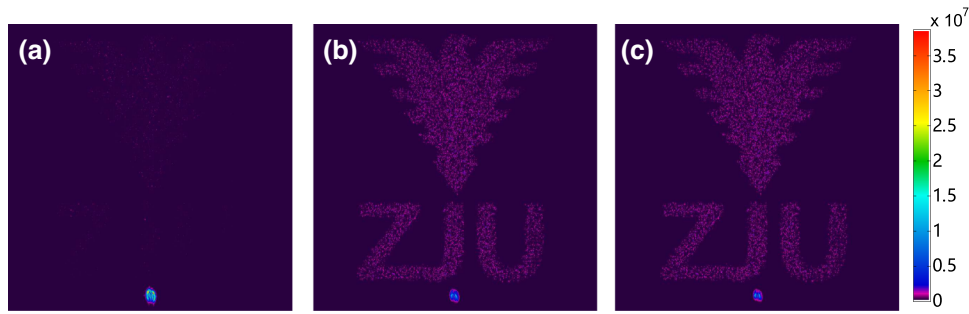


FIG. 5. The measured 2D diffraction images of ZJU eagle logo from the same hologram image with default linear phase-response curve (a) and the calibrated phase-response curve by the interferometric method (b) and the proposed one (c), respectively. Here the image values correspond to the measured intensities in all the three cases, with the same unit of the color bar.

approach in the Holoeye user guide. This method deals with fringes generated by the interference between a reference beam and a phase-modulated beam that illuminate on two different parts of the SLM: one part with a fixed input grayscale value 0 and the other part with changing values from 0 to 255. The experimental setup is referred to [16] and here we use a camera (Thorlab DCC 1545M) as required in the user guide. The calibrated phase-response curve by the interferometric approach is shown as the red rhombus line in Fig. 4(b), where the two methods show good agreement with each other. We note that there are relatively large deviations for the measured results between these two methods in the region of small phase delays, because they both have low signal sensitivity in this case. For the proposed method, one can enhance the sensitivity for small phase delay by separately measuring I_2 with a rather strong input intensity I_1 .

To show the advantages of the proposed method, Table I compares the number of shots and time consumption between the proposed method and the interferometric one. For the number of shots, the present method only needs two shots, while the interferometric one takes 256 shots of fringes corresponding to 256 grayscale values and hence it takes more time for calibration. Overall, the proposed method reduces the calibration time to 0.3 s in comparison to 14 s with the interferometric one. Further, the interferometric approach is sensitive to environmental disturbance, such that it needs to repeat the measurement process for more times to avoid drifts in space.

To test the performance, we demonstrate a holography, which shows the dramatic improvement of the diffraction efficiencies. Figure 5 shows the reconstructed images of ZJU (Zhejiang University) eagle logo with a 200-mm-focal-length lens from the same holography calculated by the iterative Gerchberg-Saxton algorithm [48]. The patterns separate the zeroth-order diffraction spots by introducing a grating function in the input hologram. Figure 5(a) represents diffraction patterns of the hologram with the default linear

phase-response curve, where the output phase delay between 0 and 2π is assumed to increase linearly with the input grayscale values between 0 and 255. With the phase-response curve calibrated by the interferometric method and the proposed one, Figs. 5(b) and 5(c) show that the intensities of the diffraction pattern become stronger. The diffraction efficiency of the zeroth-order spot is decreased by a factor of 4.8 and 5.5 times for the interferometric method and the proposed one, respectively. Since the correct phase-response curve greatly increases the signal-to-noise ratio, both of them have consistent performances, and especially the proposed method further improves the diffraction efficiency of 12.7% in comparison to the interferometric method.

IV. DISCUSSION AND CONCLUSION

We note that the present method can be straightforwardly extended to a calibration method for each single pixel. Suppose that the calibrated pixel is chosen at (x_0, y_0) . We first set the grayscale image in SLM as Fig. 2(b). Then we gradually increase the grayscale value at the upper part $y \geq y_0$ from 0 to 255 and measure the output intensity \bar{I} at (x_0, y_0) for each time T . The phase-response curve of the pixel can be computed according to Eq. (5), just by considering the variable x substituted by T . Such calibration is practical in the cases where precise control of each pixel is required, e.g., optical Ising machines using spatial light modulators [49–53].

In summary, we propose a SLM calibration method based on spatial differentiation, for either global pixels or each single one. The principle is that spatial differentiation can convert the variations in the phase delay into intensity distribution, which can be measured directly. The technique operates in short time with a simple imaging process. We use the two-beam interference approach to evaluate the performance of phase calibration and the result shows the SLM is well calibrated. Also, we show that the diffraction

efficiency of the holography is improved with the present calibration method.

ACKNOWLEDGMENTS

The authors acknowledge funding through the National Natural Science Foundation of China (NSFC Grants No. 91850108 and No. 61675179), the National Key Research and Development Program of China (Grant No. 2017YFA0205700), the Open Foundation of the State Key Laboratory of Modern Optical Instrumentation, and the Open Research Program of Key Laboratory of 3D Micro/Nano Fabrication and Characterization of Zhejiang Province. Z.R., J.H., and T.Z. are named inventors on a number of related patent applications related to this work.

-
- [1] Y. Zuo, B. Li, Y. Zhao, Y. Jiang, Y.-C. Chen, P. Chen, G.-B. Jo, J. Liu, and S. Du, All-optical neural network with nonlinear activation functions, *Optica* **6**, 1132 (2019).
- [2] J. Bueno, S. Maktoobi, L. Froehly, I. Fischer, M. Jacquot, L. Larger, and D. Brunner, Reinforcement learning in a large-scale photonic recurrent neural network, *Optica* **5**, 756 (2018).
- [3] T. Zhu, Y. Zhou, Y. Lou, H. Ye, M. Qiu, Z. Ruan, and S. Fan, Plasmonic computing of spatial differentiation, *Nat. Commun.* **8**, 1 (2017).
- [4] T. Zhu, Y. Lou, Y. Zhou, J. Zhang, J. Huang, Y. Li, H. Luo, S. Wen, S. Zhu, Q. Gong, *et al.*, Generalized Spatial Differentiation from the Spin Hall Effect of Light and Its Application in Image Processing of Edge Detection, *Phys. Rev. Appl.* **11**, 034043 (2019).
- [5] T. Zhu, J. Huang, and Z. Ruan, Optical phase mining by adjustable spatial differentiator, *Adv. Photonics* **2**, 1 (2020).
- [6] O. Mendoza-Yero, G. Mínguez-Vega, and J. Lancis, Encoding complex fields by using a phase-only optical element, *Opt. Lett.* **39**, 1740 (2014).
- [7] J. Leach, B. Jack, J. Romero, A. K. Jha, A. M. Yao, S. Franke-Arnold, D. G. Ireland, R. W. Boyd, S. M. Barnett, and M. J. Padgett, Quantum correlations in optical angle-orbital angular momentum variables, *Science* **329**, 662 (2010).
- [8] D. G. Grier, A revolution in optical manipulation, *Nature* **424**, 810 (2003).
- [9] J. E. Curtis, B. A. Koss, and D. G. Grier, Dynamic holographic optical tweezers, *Opt. Commun.* **207**, 169 (2002).
- [10] M. R. Beversluis, L. Novotny, and S. J. Stranick, Programmable vector point-spread function engineering, *Opt. Express* **14**, 2650 (2006).
- [11] A. Lubatsch and R. Frank, Self-consistent quantum field theory for the characterization of complex random media by short laser pulses, *Phys. Rev. Res.* **2**, 013324 (2020).
- [12] A. Lubatsch and R. Frank, Evolution of floquet topological quantum states in driven semiconductors, *Eur. Phys. J. B* **92**, 215 (2019).
- [13] A. Lubatsch and R. Frank, Behavior of Floquet topological quantum states in optically driven semiconductors, *Symmetry* **11**, 1246 (2019).
- [14] A. Lubatsch and R. Frank, Quantum many-body theory for exciton-polaritons in semiconductor Mie resonators in the non-equilibrium, *Appl. Sci.* **10**, 1836 (2020).
- [15] R. Frank, Coherent control of Floquet-mode dressed plasmon polaritons, *Phys. Rev. B* **85**, 195463 (2012).
- [16] A. Bergeron, J. Gauvin, F. Gagnon, D. Gingras, H. H. Arsenault, and M. Doucet, Phase calibration and applications of a liquid-crystal spatial light modulator, *Appl. Opt.* **34**, 5133 (1995).
- [17] S. Reichelt, Spatially resolved phase-response calibration of liquid-crystal-based spatial light modulators, *Appl. Opt.* **52**, 2610 (2013).
- [18] X. Xun and R. W. Cohn, Phase calibration of spatially nonuniform spatial light modulators, *Appl. Opt.* **43**, 6400 (2004).
- [19] J. Otón, P. Ambs, M. S. Millán, and E. Pérez-Cabré, Multipoint phase calibration for improved compensation of inherent wavefront distortion in parallel aligned liquid crystal on silicon displays, *Appl. Opt.* **46**, 5667 (2007).
- [20] G. Rajshekhar, B. Bhaduri, C. Edwards, R. Zhou, L. L. Goddard, and G. Popescu, Nanoscale topography and spatial light modulator characterization using wide-field quantitative phase imaging, *Opt. Express* **22**, 3432 (2014).
- [21] J. L. M. Fuentes, E. J. Fernández, P. M. Prieto, and P. Artal, Interferometric method for phase calibration in liquid crystal spatial light modulators using a self-generated diffraction-grating, *Opt. Express* **24**, 14159 (2016).
- [22] L. Turquet, M. Kauranen, and G. Bautista, Phase Calibration of Liquid-Crystal-Based Spatial Light Modulators Using the Spatial Structure of Focused Optical Fields, *Phys. Rev. Appl.* **11**, 044050 (2019).
- [23] Z. Zhang, G. Lu, and T. Francis, Simple method for measuring phase modulation in liquid crystal televisions, *Opt. Eng.* **33**, 3018 (1994).
- [24] D. Engström, M. Persson, J. Bengtsson, and M. Goksör, Calibration of spatial light modulators suffering from spatially varying phase response, *Opt. Express* **21**, 16086 (2013).
- [25] F. P. Ferreira and M. S. Belsley, Direct calibration of a spatial light modulator by lateral shearing interferometry, *Opt. Express* **18**, 7899 (2010).
- [26] L. Martínez-León, Z. Jaroszewicz, A. Kołodziejczyk, V. Durán, E. Tajahuerce, and J. Lancis, Phase calibration of spatial light modulators by means of fresnel images, *J. Opt. A: Pure Appl. Opt.* **11**, 125405 (2009).
- [27] A. Silva, F. Monticone, G. Castaldi, V. Galdi, A. Alù, and N. Engheta, Performing mathematical operations with metamaterials, *Science* **343**, 160 (2014).
- [28] S. AbdollahRamezani, K. Arik, A. Khavasi, and Z. Kavehvasht, Analog computing using graphene-based metalines, *Opt. Lett.* **40**, 5239 (2015).
- [29] A. Chizari, S. Abdollahramezani, M. V. Jamali, and J. A. Salehi, Analog optical computing based on a dielectric meta-reflect array, *Opt. Lett.* **41**, 3451 (2016).
- [30] A. Pors, M. G. Nielsen, and S. I. Bozhevolnyi, Analog computing using reflective plasmonic metasurfaces, *Nano Lett.* **15**, 791 (2015).
- [31] Y. Hwang, T. J. Davis, J. Lin, and X.-C. Yuan, Plasmonic circuit for second-order spatial differentiation at the subwavelength scale, *Opt. Express* **26**, 7368 (2018).

- [32] H. Kwon, D. Sounas, A. Cordaro, A. Polman, and A. Alù, Nonlocal Metasurfaces for Optical Signal Processing, *Phys. Rev. Lett.* **121**, 173004 (2018).
- [33] J. Zhou, H. Qian, C.-F. Chen, J. Zhao, G. Li, Q. Wu, H. Luo, S. Wen, and Z. Liu, Optical edge detection based on high-efficiency dielectric metasurface, *Proc. Natl. Acad. Sci.* **116**, 11137 (2019).
- [34] T. J. Davis, F. Eftekhari, D. E. Gómez, and A. Roberts, Metasurfaces with Asymmetric Optical Transfer Functions for Optical Signal Processing, *Phys. Rev. Lett.* **123**, 013901 (2019).
- [35] A. Cordaro, H. Kwon, D. Sounas, A. F. Koenderink, A. Alù, and A. Polman, High-index dielectric metasurfaces performing mathematical operations, *Nano Lett.* **19**, 8418 (2019).
- [36] A. Momeni, H. Rajabalipanah, A. Abdolali, and K. Achouri, Generalized Optical Signal Processing Based on Multioperator Metasurfaces Synthesized by Susceptibility Tensors, *Phys. Rev. Appl.* **11**, 064042 (2019).
- [37] A. Youssefi, F. Zangeneh-Nejad, S. Abdollahramezani, and A. Khavasi, Analog computing by Brewster effect, *Opt. Lett.* **41**, 3467 (2016).
- [38] L. L. Doskolovich, D. A. Bykov, E. A. Bezus, and V. A. Soifer, Spatial differentiation of optical beams using phase-shifted Bragg grating, *Opt. Lett.* **39**, 1278 (2014).
- [39] Z. Dong, J. Si, X. Yu, and X. Deng, Optical spatial differentiator based on subwavelength high-contrast gratings, *Appl. Phys. Lett.* **112**, 181102 (2018).
- [40] C. Guo, M. Xiao, M. Minkov, Y. Shi, and S. Fan, Photonic crystal slab laplace operator for image differentiation, *Optica* **5**, 251 (2018).
- [41] C. Guo, M. Xiao, M. Minkov, Y. Shi, and S. Fan, Isotropic wavevector domain image filters by a photonic crystal slab device, *J. Opt. Soc. Am. A* **35**, 1685 (2018).
- [42] W. Wu, W. Jiang, J. Yang, S. Gong, and Y. Ma, Multi-layered analog optical differentiating device: Performance analysis on structural parameters, *Opt. Lett.* **42**, 5270 (2017).
- [43] W. Zhang and X. Zhang, Backscattering-Immune Computing of Spatial Differentiation by Nonreciprocal Plasmonics, *Phys. Rev. Appl.* **11**, 054033 (2019).
- [44] Z. Ruan, Spatial mode control of surface plasmon polariton excitation with gain medium: From spatial differentiator to integrator, *Opt. Lett.* **40**, 601 (2015).
- [45] Y. Fang, Y. Lou, and Z. Ruan, On-grating graphene surface plasmons enabling spatial differentiation in the terahertz region, *Opt. Lett.* **42**, 3840 (2017).
- [46] Y. Fang and Z. Ruan, Optical spatial differentiator for a synthetic three-dimensional optical field, *Opt. Lett.* **43**, 5893 (2018).
- [47] K. Y. Bliokh, F. J. Rodríguez-Fortuño, F. Nori, and A. V. Zayats, Spin-orbit interactions of light, *Nat. Photonics* **9**, 796 (2015).
- [48] R. Gerekberg and W. Saxton, A practical algorithm for the determination of phase from image and diffraction plane pictures, *Optik* **35**, 237 (1972).
- [49] D. Pierangeli, G. Marcucci, and C. Conti, Large-Scale Photonic Ising Machine by Spatial Light Modulation, *Phys. Rev. Lett.* **122**, 213902 (2019).
- [50] D. Pierangeli, G. Marcucci, D. Brunner, and C. Conti, arXiv:2004.02208v1 [Nanophotonics (to be published)].
- [51] D. Pierangeli, G. Marcucci, and C. Conti, arXiv:2005.08690.
- [52] D. Pierangeli, M. Rafayelyan, C. Conti, and S. Gigan, arXiv:2006.00828.
- [53] S. Kumar, H. Zhang, and Y.-P. Huang, Large-scale ising emulation with four body interaction and all-to-all connections, *Commun. Phys.* **3**, 1 (2020).